

# 1 The optics of the human eye at 8.6 2 $\mu\text{m}$ lateral resolution

3 Sergio Bonaque-González\*<sup>1</sup>, Juan M. Trujillo-Sevilla<sup>1</sup>, Miriam Velasco-Ocaña<sup>1</sup>,  
4 Óscar Casanova-González<sup>1</sup>, Miguel Sicilia-Cabrera<sup>1</sup>, Alex Roqué-Velasco<sup>1</sup>, Sabato  
5 Ceruso<sup>1</sup>, Ricardo Oliva-García<sup>1</sup>, Javier Martín-Hernández<sup>1</sup>, Oscar Gomez-  
6 Cardenes<sup>1</sup>, José G. Marichal-Hernández<sup>1</sup>, Damien Gatinel<sup>2</sup>, Jack T. Holladay<sup>3</sup>,  
7 José M. Rodríguez-Ramos<sup>1\*</sup>

8 1. Woptix S.L. Avda, Trinidad 61 planta 7, La Laguna, Tenerife, Canary  
9 Islands. Spain

10 2. Rothschild Foundation Hospital, 29 Rue Manin, Paris, France,

11 3. Baylor College of Medicine, Houston, TX, USA

12

13 \* Corresponding authors:

14 Sergio Bonaque-González: Woptix S.L. Avda, Trinidad 61 planta 7,  
15 38204 La Laguna, Tenerife, Canary Islands. Spain.  
16 sergiob@woptix.com 0034682121870

17 José M. Rodríguez-Ramos: Woptix S.L. Avda, Trinidad 61 planta 7,  
18 38204 La Laguna, Tenerife, Canary Islands. Spain.  
19 jmramos@woptix.com 0034619177299

20

21

22

23

24

25

26

27 NOTE: This preprint reports new research that has not been certified by peer review and should not be used to guide clinical practice.

## 28 **Abstract**

---

29           Ocular optics is normally estimated based on 2,600 measurement  
30 points within the pupil of the eye, which implies a lateral resolution of  
31 approximately 175 microns for a 9 mm pupil diameter. This is because  
32 information below this resolution is not thought to be relevant or even  
33 possible to obtain with current measurement systems. In this work, we  
34 characterize the in vivo ocular optics of the human eye with a lateral  
35 resolution of 8.6 microns, which implies roughly 1 million measurement  
36 points for a pupil diameter of 9 mm. The results suggest that the  
37 normal human eye presents a series of hitherto unknown optical  
38 patterns with amplitudes between 200 and 300 nm and is made up of a  
39 series of in-phase peaks and valleys. If the results are analysed at only  
40 high lateral frequencies, the human eye is also found to contain a  
41 whole range of new information. This discovery could have a great  
42 impact on the way we understand some fundamental mechanisms of  
43 human vision and could be of outstanding utility in certain fields of  
44 ophthalmology.

45

46

47

48

49

50

## 51 **Introduction**

---

52 Knowledge of the optics of the human eye has allowed us to broaden  
53 the understanding of the mechanism of human vision. It has led the  
54 current field of ophthalmology to a highly technical level where  
55 customized treatments and instrumentation-based diagnostics have  
56 become the norm. However, measuring the optics of the eye is not a  
57 trivial task. In 1961, Smirnov developed an advanced version of the  
58 Scheiner disk [1] to subjectively estimate the optical imperfections of  
59 the eye, also called aberrations or phase map, in a process named  
60 ocular aberrometry [2]. At that time, he anticipated that his invention  
61 would have no practical application, stating that "...the calculations  
62 take 10–12 hours [...] Therefore, it is unlikely that such detailed  
63 measurements will ever be adopted by practitioner-ophthalmologists."  
64 He did not foresee that advances in computer science would greatly  
65 speed up calculations and that scientists would find the measurement  
66 of ocular aberrations an invaluable tool, progressing from a research  
67 instrument to a clinical application system. Indeed, some of modern  
68 ophthalmology could not be understood without the deep  
69 understanding of ocular optics that aberrometers have made possible.

70 Currently, there are several options for the estimation of ocular  
71 aberrations based on different techniques, i.e., Hartmann-Shack  
72 sensors (H-S) [3], pyramidal sensors (P-S) [4], interferometric  
73 techniques [5], laser ray tracing [6] and curvature sensors [7].  
74 Techniques based on H-S sensors are the most widely used in  
75 ophthalmology. However, they are restricted to sampling the phase

76 map at up to 2,600 measurement points within the pupil of the eye  
77 (approximately 175  $\mu\text{m}$  of lateral resolution for a 9 mm pupil diameter  
78 [8]) and also suffer from a limited dynamic range [9]. These limitations  
79 constrain its usefulness in abnormal eyes, which are precisely the most  
80 interesting to characterize [10]. Currently, P-S offers the highest  
81 resolution in ocular aberrometry, up to 45,000 measurement points  
82 (approximately 37  $\mu\text{m}$  theoretical lateral resolution for a 9 mm pupil  
83 diameter) [8]. Nevertheless, P-S generally suffers from non-linear  
84 behaviour, diffraction effects between its different pupil images, and a  
85 relatively limited dynamic range as a result of the trade-off between  
86 the slope accuracy and achievable spatial resolution [11]. These  
87 drawbacks cause the phase maps obtained to be somewhat fuzzy, and  
88 the details that can be visualized do not match the theoretical  
89 resolution [8]. Therefore, the H-S sensor is still considered the gold  
90 standard in ophthalmology.

91 Actual knowledge about the optics of the normal human eye can be  
92 roughly summarized as follows: it has relatively smooth optics with no  
93 optical structures that diverge too greatly from a conical shape with  
94 some astigmatism. Its phase map is usually expressed as a  
95 decomposition of orthonormal polynomials within a circular pupil, in  
96 particular Zernike polynomials [12], where most of the deformations  
97 can be described with the first two to three dozen terms [13, 14]. Thus,  
98 up to 66 Zernike terms are usually considered sufficient to represent  
99 ocular optics with high quality even in pathological eyes, assuming a  
100 loss of high frequencies that is not considered to hide any relevant

101 information. [15, 16]. However, some authors have already drawn  
102 attention to the inefficiency of this approach [17].

103 In this work, we characterize the ocular optics of living human eyes  
104 with a lateral resolution of approximately 8.55  $\mu\text{m}$ . This implies more  
105 than a million points of measurement for a pupil with a diameter of 9  
106 mm, orders of magnitude higher than the current gold standard  
107 offered by the H-S sensor. We show evidence that when ocular optics  
108 are measured at a sufficiently high resolution, a series of phase  
109 structures emerge. We hypothesize that this finding could have a great  
110 impact on some current ophthalmic surgical procedures and on the  
111 clarification of some fundamental mechanisms of human vision.

112

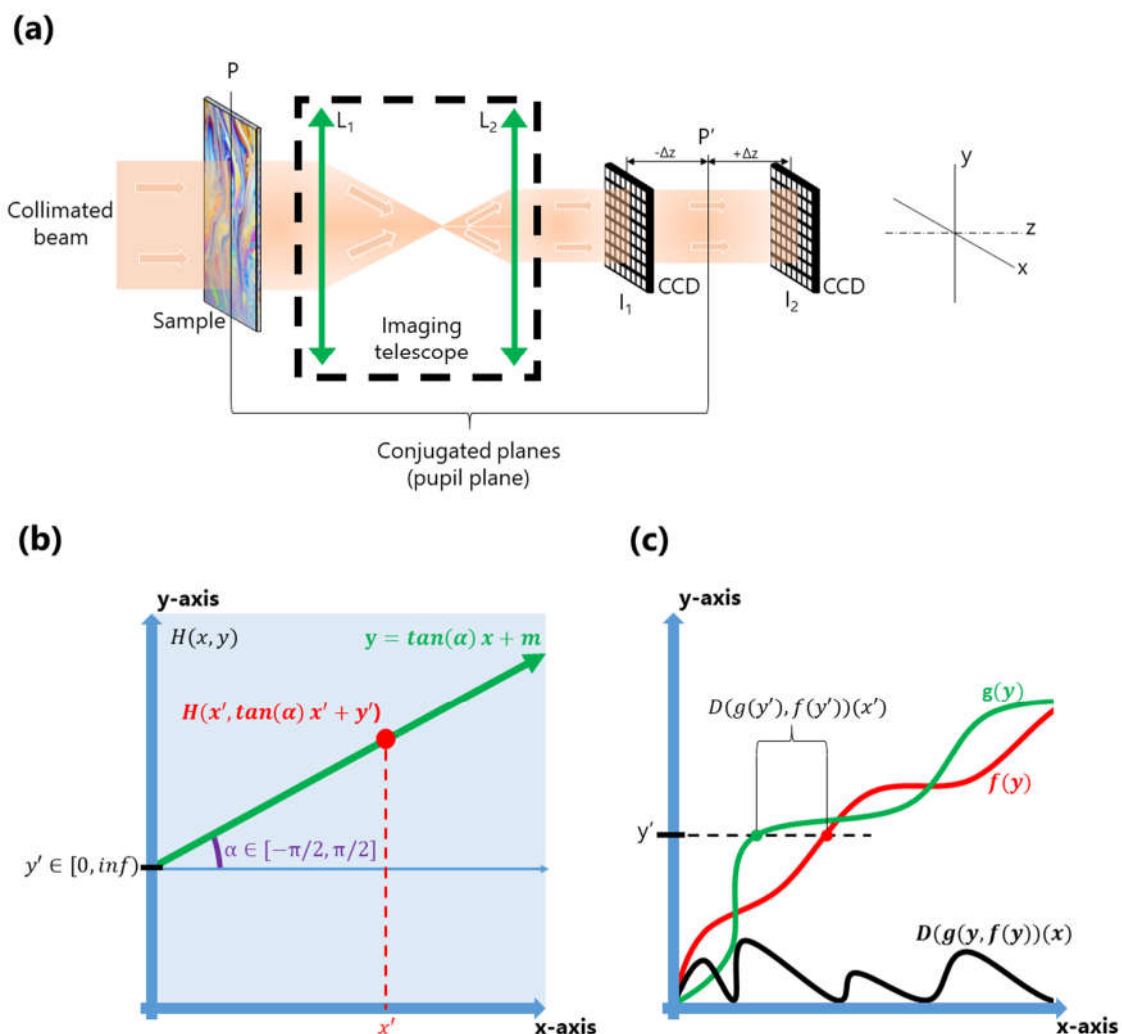
## 113 **Methods**

---

### 114 **The phase sensor**

115 To measure the phase map, we use the wavefront phase imaging  
116 (WFPI) sensor, which offers high resolution and has been used with  
117 success in other fields, such as semiconductor silicon metrology [18].  
118 WFPI captures two intensity images around the pupil plane of the  
119 instrument using a standard image sensor, i.e., a charge-coupled  
120 device (CCD). Then, the phase gradients along two orthogonal  
121 directions are recovered from both the captured intensity distributions.  
122 A standard WFPI setup for transparent samples is depicted in figure 1a.  
123 A collimated beam (with an almost flat phase map) from a light-  
124 emitting diode (LED) is used as the light source. The use of incoherent  
125 light, in contrast to the H-S sensor, makes this sensor insensitive to

126 speckle effects. The light beam passes through the sample, which  
 127 modifies the shape of the beam according to the optical behaviour of  
 128 the sample, thus generating a distorted outgoing phase map. An  
 129 imaging telescope composed of a pair of converging lenses,  $L_1$  and  $L_2$ ,  
 130 translates the plane of the sample,  $P$ , into a conjugated plane,  $P'$ . The  
 131 two required intensity images,  $I_1$  and  $I_2$ , are acquired around  $P'$  in  
 132 equidistant planes along the  $z$ -axis. Choosing focal lengths of  $L_1$  and  $L_2$   
 133 appropriately allows us to adjust the sample size to the sensor size.  
 134 This optical setup is similar to some proposals for curvature sensors [7];  
 135 however, the mathematical treatment of the data in WFPI is completely  
 136 different, as explained below.



137

138 Figure 1. (a) Basic optical setup of the wavefront phase intensity (WFPI)  
139 technique for transparent samples; (b) graphical representation of Eq.  
140 1; (c) graphical representation of Eq. 2. P: pupil plane; L: lens; I: intensity  
141 image; CCD: charge-coupled device; P': conjugated pupil plane.

142 Let  $H(x, y)$  be a continuous two-dimensional function defined for  
143 positive values of  $x, y$  and taking only positive numbers as values, and  
144 let  $V$  be an auxiliary transformation function acting on  $H$  as follows:

$$V(H_{y,\alpha})(x) = \int_0^x H(x, \tan(\alpha)x + y) \text{ for } \begin{cases} x \in [0, \infty) \\ \forall y \in [0, \infty) \\ \forall \alpha \in \{-\pi/2, \pi/2\} \end{cases} \quad (1)$$

145  
146 where  $\alpha$  is a variable composed of a set of  $k$  discrete angles uniformly  
147 distributed in the interval  $[-\pi/2, \pi/2]$ , each defining a line with its origin  
148 in  $y$  and an angular separation from the  $x$  – axis equal to  $\alpha$  (see figure  
149 1b). Then, for each pair of values  $y$  and  $\alpha$ ,  $V(H_{y,\alpha})(x)$  is a one-dimensional  
150 function that represents the accumulated  $H(x, y)$  values along the  
151 defined line of  $H$ . The graphical representation of  $V(x)$  for particular  
152 values of  $(y, \alpha)$  is similar to one of the coloured curves, green or red, in  
153 figure 1c.

154 Let  $D$  be another auxiliary function that represents the distance on the  
155 abscissa axis between two unidimensional continuous functions  
156 represented by  $f(x)$  and  $g(x)$ , defined for positive values of  $x$  and  
157 yielding only positive numbers. Figure 1c shows a graphical  
158 representation of  $D$ , which can be mathematically described as:

$$D(f, g)(x) = \underset{x}{\operatorname{argmin}}(f(x) - y) - \underset{x}{\operatorname{argmin}}(g(x) - y) \text{ for } y \in [0, \infty). \quad (2)$$

159 Let  $I_1(x, y)$  and  $I_2(x, y)$  be two continuous bi-dimensional functions  
160 representing two different intensity maps from which it is desired to  
161 recover the phase map. The phase gradients in the horizontal and  
162 vertical directions,  $\varphi_h$  and  $\varphi_v$ , are directly related to  $I_1$  and  $I_2$  as follows:

163

$$\varphi_h(x, y) = \frac{1}{k} \sum_{\alpha=-\frac{\pi}{2}}^{\alpha=\frac{\pi}{2}} \cos(\alpha) D(V(I_{1(y,\alpha)}, V(I_{2(y,\alpha)})) (x) \quad (3)$$

$$\varphi_v(x, y) = \frac{1}{k} \sum_{\alpha=-\frac{\pi}{2}}^{\alpha=\frac{\pi}{2}} \sin(\alpha) D(V(I_{1(y,\alpha)}, V(I_{2(y,\alpha)})) (x) \quad (4)$$

164 where  $k$  is the number of discrete angles considered, defined as:

$$k = \left| -\frac{\pi}{2}, \frac{\pi}{2} \right| \quad (5)$$

165

166 Note that the units of  $\varphi_h$  and  $\varphi_v$  correspond to those of the input  
167 intensity images, i.e., pixels. To convert these units into physical units,  
168 i.e., metres, we apply a factor that takes into account the pixel size,  $s$ ,  
169 and the distance between the images,  $2\Delta z$ :

$$\varphi'_h(x, y) = \frac{s^2}{2\Delta z} \varphi_h(x, y) \quad (6)$$

$$\varphi'_v(x, y) = \frac{s^2}{2\Delta z} \varphi_v(x, y) \quad (7)$$

170

171 Finally, numerical integration is required to obtain the phase map from  
172 its derivatives. In our case, we use the algorithm developed by Talmi &

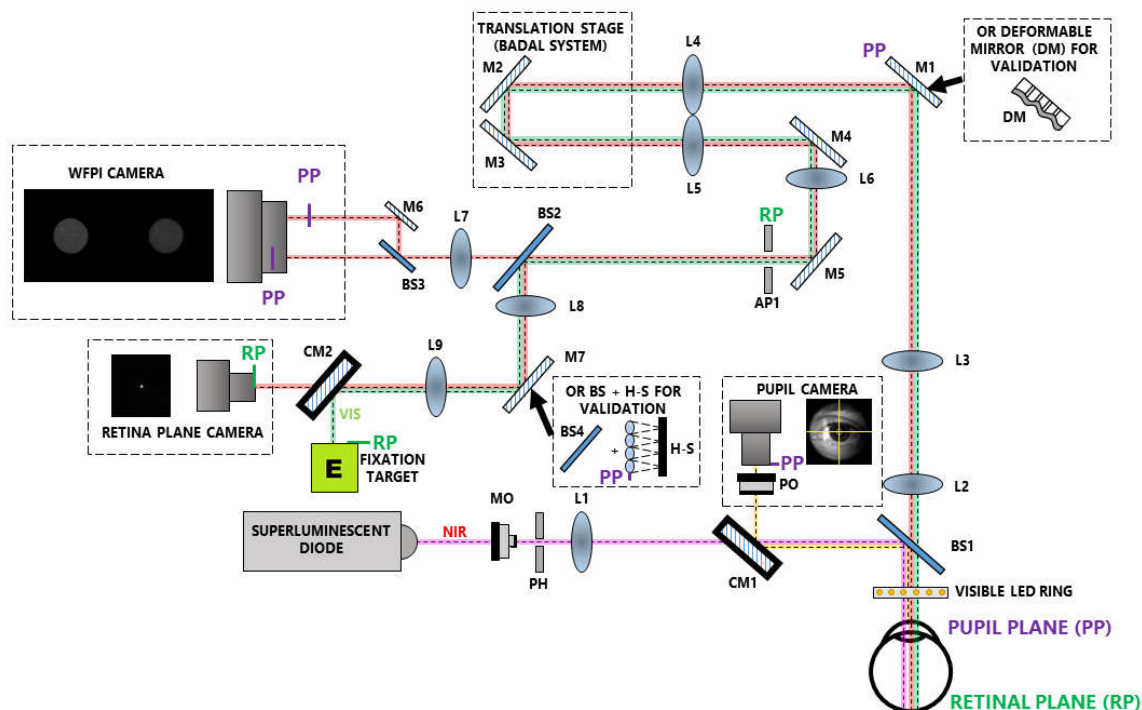
173 Ribal [19]; however, very similar results can be obtained using other  
174 methods [20].

175 For simplicity, the above mathematical equations have been made  
176 assuming continuous functions, but the same reasoning can be  
177 followed for a real implementation where  $I_1$  and  $I_2$  are discrete and  
178 finite intensity image maps. In this case, it would be necessary to apply  
179 affine transformations to functions  $D$  and  $V$  to be able to deal with the  
180 discrete nature of the real intensity images, which can be done  
181 computationally in an intuitive way through interpolation. Regarding  
182 the value of  $k$ , we did not find a significant increase in the precision of  
183 the algorithm when  $k > 120$  for resolution  $\leq 4096 \times 4096$  and pixel  
184 size  $\approx 9\mu m$ . However, with other configurations, the optimal value of  $k$   
185 should be studied. This is a generalized and formal explanation of the  
186 WFPI basis, and its computational implementation is simpler. We  
187 encourage the interested reader to consult the step-by-step  
188 explanation of the algorithm in patent PCT/EP2018/052533 [21], which  
189 is more focused on the computational and discrete aspects of the  
190 methodology.

191

## 192 **The apparatus**

193 Measurements were performed in a custom-developed double-pass  
194 optical setup incorporating a WFPI implementation. Its current  
195 configuration, outlined in figure 2, has 4 different channels:



196

197 Figure 2. Schematic diagram of a custom-made optical system with 4  
 198 different channels: (1) the illumination channel (pink line); (2) the pupil  
 199 monitoring channel (yellow line); (3) the science channel (red line); and  
 200 (4) the fixation target channel (green line). NIR: near infrared light; MO:  
 201 microscope objective; PH: pinhole; L: lens; CM: cold mirror; PO:  
 202 photographic objective; BS: beam splitter; M: mirror; AP: aperture; H-S:  
 203 Hartmann-Shack sensor; VIS: visible light.

204

205 (1) The illumination channel contains a single-mode  
 206 superluminescent diode (SLD) (QSDM-780-15D, QPhotonics,  
 207 LLC, Ann Arbor, USA) with a central wavelength ( $\lambda$ ) of 780 nm  
 208 and a spectral bandwidth of 20 nm. It works in combination with  
 209 a control unit (CLD1015, Thorlabs, Newton, USA) that allows the  
 210 maximum emission time to be set at 35 ms. The microscope

211 objective focuses light into a pinhole that removes aberrant rays.  
212 Then, an achromatic lens is placed with its back focal point in the  
213 pinhole to obtain a collimated (nearly parallel) beam. After  
214 passing through a cold mirror and a non-polarizing 10:90 beam  
215 splitter, the beam is directed towards the eye with a beam  
216 diameter of approximately 800  $\mu\text{m}$ . An offset of the beam from  
217 the centre of the pupil is introduced to avoid corneal reflections  
218 in the WFPI intensity images. The maximum permissible  
219 exposure in the pupil plane for 35 ms at  $\lambda=780$  nm is 2.4 mW,  
220 which is calculated using the safety limits of the ANSI standards  
221 for the wavelength used [22]. We measured 0.78 mW in the  
222 pupil plane, which is well below the ANSI safety standards.

223 (2) The pupil monitoring channel allows the position of the subject to  
224 be monitored during the measurements. It consists of a  
225 monochrome camera (UI-3370SE-M-GL, IDS, Obersulm, Germany)  
226 in combination with a camera lens that conjugates the pupil plane  
227 of the system with that of the camera. A ring with 18 small LEDs of  
228  $\lambda=630$  nm placed before the eye provides the illumination for this  
229 channel. Its light power measured in the corneal plane is orders of  
230 magnitude below the ANSI standard safety limits for the  
231 wavelength used.

232 (3) The science channel. The retina spreads the incoming light from  
233 channel 1 from back to front. When the dispersed light beam  
234 emerges from the eye, it will carry the phase information for the  
235 entire eye, including the cornea and the lens. This beam is guided

236 through a variety of converging lenses to adjust the beam size to  
237 the WFPI camera size and to correct for defocus in the Badal system  
238 in a range of [-10.00 +10.00] D. As the presence of defocus will  
239 change the size of the intensity images in the WFPI, its correction  
240 by the Badal system allows us to provide an almost constant lateral  
241 resolution between eyes with different spherical refractions. A  
242 monochromatic camera positioned in the retinal plane (UI-3370SE-  
243 M-GL, IDS, Obersulm, Germany) allows us to estimate the Badal  
244 position that offers the best spherical correction by maximizing the  
245 central intensity of the focused light beam. In the event of an error  
246 in the correction process of the Badal system, it is shown by specific  
247 measurements that residual defocus values can be characterized by  
248 the WFPI sensor in a range of  $\pm 6.00$  D. An aperture is placed in a  
249 retina plane to reduce reflections within the system. To capture two  
250 intensity images around the pupil plane of the eye at a separation  
251 of 13.33 mm, a small system composed of a 50:50 beam splitter  
252 and a mirror divides the science beam into two parts, which are  
253 simultaneously captured by a low-noise, 11-megapixel cooled  
254 camera (Bigeye G-1100 Cool, Allied Vision Technologies, Stadtroda,  
255 Germany). The magnification of the apparatus is approximately  
256 1.0523, and each pixel in the estimated phase map represents  
257 approximately  $8.553 \mu\text{m}$  in the plane of the pupil of the eye.

258 (4) The fixation target channel consists of a modified liquid crystal  
259 display (LCD) retro-illuminated monochromatically at  $\lambda=620$  nm.  
260 The projected image is a binary Maltese cross that can be more  
261 clearly observed by the experimental subject once the Badal system

262 has made the spherical correction. The centre of the cross is  
263 coincident with the optical axis of the system, so that when the  
264 subject fixes on it, the optical axis of the system is aligned with the  
265 line of sight. Its light power measured in the corneal plane is orders  
266 of magnitude below the ANSI standard safety limits for the  
267 wavelength used.

268 For calibration and validation of the system (see next section), an H-S  
269 sensor (WFS20-5C, Thorlabs, Newton, USA) and/or a deformable mirror  
270 (DM) (DM140A-35-UP01; Boston Micromachines, Boston, USA) were  
271 placed in the pupil planes within the system, as depicted in figure 2.

272 The optical setup was mounted on an x-y-z translation stage that was  
273 manually controlled by a joystick to align the pupil of the eye with the  
274 instrument using the pupil-monitoring channel. A conventional  
275 ophthalmic chinrest intended to position the experimental subject was  
276 attached to the table that supported the entire instrument.

277 All the optoelectronic and mechanical elements of the apparatus were  
278 automatically controlled and synchronized using custom-built software  
279 in C++. All processing of the H-S and WFPI intensity images was  
280 performed using custom-built software in MATLAB (v2019a,  
281 MathWorks Inc., Natick, USA).

282 The WFPI software provides the phase map within the actual pupil of  
283 the measured element, which can be circular or not. When measuring  
284 at a high resolution, the fit to the Zernike polynomials does not provide  
285 a good physical representation of the object under study [17].

286 Nevertheless, in all cases, a Zernike adjustment was made for

287 compatibility with the H-S sensor used for validation and to split the  
288 overall phase error into the main Zernike components. The required  
289 circular pupil defined for this fitting was the largest one inscribed  
290 within the real pupil when not specified otherwise.

291

## 292 **Calibration and validation**

293 For the calibration of the prototype, a custom-designed eye model,  
294 composed of an artificial retina rotating at 300 rpm, an artificial cornea  
295 (an achromatic doublet with a focal length of 40 mm), and an artificial  
296 pupil with a 7 mm diameter, was placed in the measurement position.  
297 All the components of the eye model shared the same optical axis. Its  
298 emmetropic condition, when needed, was calibrated with a shearing  
299 interferometer (SI100, Thorlabs, Newton, USA). A series of defocuses  
300 was induced by increasing or decreasing the distance between the  
301 retina and the cornea of the artificial eye, in a range of  
302 approximately -7.00 to 7.00 D in 13 steps. The defocus status of the  
303 artificial eye was determined by independent measurement (outside  
304 the apparatus) with the H-S sensor using a small optical assembly  
305 designed for this purpose. Additionally, cylindrical trial lenses of +0.50,  
306 +1.00, +2.00 and +3.00 D with axes of 90, 45, and 22° were centred in  
307 front of the emmetropic artificial eye with back vertex distances of 5  
308 mm. The measurements were recorded with respect to the pupil plane  
309 and compared to the powers of the trial lenses, transferring the  
310 obtained power from the pupil plane to the trial lens plane. For both  
311 conditions, defocus and astigmatism, the phase map was estimated

312 using the WFPI sensor by taking 3 consecutive measurements. The  
313 defocus or astigmatism in diopters was calculated from the obtained  
314 phase maps by decomposing it into Zernike polynomials and using the  
315 methodology proposed by Salmon T. et al. [23], with the difference that  
316 half of the cylindrical value was not added to the value of the sphere to  
317 facilitate the determination of the origin of possible errors.

318 The repeatability of the instrument was tested by using the  
319 “continuous”-mode capturing option of the science camera, which  
320 acquires an intensity image approximately once per second (even  
321 though the exposure time can be much shorter). One hundred  
322 consecutive images were taken with the eye model with a 7 mm pupil  
323 diameter in which a slight fixed defocus was induced by manually  
324 moving the position of the retina. For the reproducibility tests, we  
325 made measurements under the same conditions, but two technicians  
326 took turns performing the measurements alternately, misaligning and  
327 realigning the device between each measurement. The results are  
328 reported in terms of the root-mean-square (RMS) error. Additionally,  
329 each individual phase map was decomposed into the first 66 Zernike  
330 polynomials according to the OSA standards [24] without considering  
331 the piston or the tip/tilt. The analysis in terms of the RMS error is  
332 shown for low-order (Zernikes 3 to 5), medium-order (Zernikes 6 to 14),  
333 and high-order (Zernikes from 15 to 65) aberrations.

334 For validation in the presence of higher frequencies (high-order  
335 aberrations), a DM was placed in a pupil plane (see figure 2) and  
336 directed with 800 phase maps with amplitudes uniformly ranging

337 between 0.35 and 2.8  $\mu\text{m}$  in 0.35  $\mu\text{m}$  steps. The phase maps that fed  
338 the DM were composed of the random values of the first 66 Zernike  
339 polynomials (piston and tip/tilt were not included). For this test, the H-  
340 S sensor was placed in a pupil plane within the setup (see figure 2) to  
341 simultaneously estimate the phase. The pupil diameter was restricted  
342 to 4 mm due to the small size of the aperture of the DM (4.4 mm). To  
343 make comparisons between the sensors possible, the phase maps  
344 obtained by both sensors were resampled to the DM input resolution  
345 by bilinear interpolation. The images in each measurement were bias-  
346 subtracted and flat-fielded (with the DM in its resting position). The  
347 results in terms of RMS errors were statistically analysed in Microsoft  
348 Excel 2016 (Microsoft, Redmond, WA) by means of the two-tailed  
349 Student's t-test (two-sided).

### 350 **In vivo tests**

351 Finally, five living human eyes belonging to five subjects aged between  
352 27 and 38 years were tested monocularly with the apparatus and with  
353 the H-S sensor placed in the system, as depicted in figure 2, in order to  
354 simultaneously obtain a reference map. The exposure time for each of  
355 the measurements was 30 ms. First, the repeatability/reproducibility in  
356 a real eye was estimated by taking 20 "consecutive" measurements,  
357 allowing the volunteer to blink between measurements, with a time  
358 between measurements of approximately 3 seconds. Second, simple  
359 measurements were taken with the apparatus for the remaining 4 eyes.  
360 All the eyes tested had a best corrected visual acuity of 20/20 or better  
361 and had no observable pathology. These eyes were not chosen for  
362 having any specific characteristics and correspond to volunteers from

363 the research laboratory itself. As the instrument is capable of taking  
364 images in 30 ms, cycloplegia was not used, and nor was a bit-bar  
365 required to take the measurements. The images in each measurement  
366 were bias-subtracted and flat-fielded. The subjects were aligned with  
367 the instrument using the x-y-z stage, while the natural pupil was  
368 viewed on a monitor using the pupil camera. As in the previous case, a  
369 simple estimation of the spherocylindrical correction was carried out  
370 using the same methodology as described above.

371 When the results of both sensors, the WFPI and H-S, were compared,  
372 the phase map obtained by WFPI was resampled to the H-S resolution  
373 by bilinear interpolation, and both maps, the H-S and WFPI, were  
374 decomposed into the first 66 Zernike polynomials. Since the pupils of  
375 real eyes are not perfectly circular, the H-S edge microlenses and their  
376 corresponding areas in WFPI were removed from processing to ensure  
377 the measurement of an area completely covered by the microlenses.

378 This study was approved by the Ethics Committee of the Hospital  
379 Universitario de Canarias, was conducted in accordance with the  
380 provisions of the Declaration of Helsinki, all volunteers were acquainted  
381 with the nature and possible consequences of the study, and provided  
382 written informed consent. Also, all subjects gave their consent for the  
383 publication of the data.

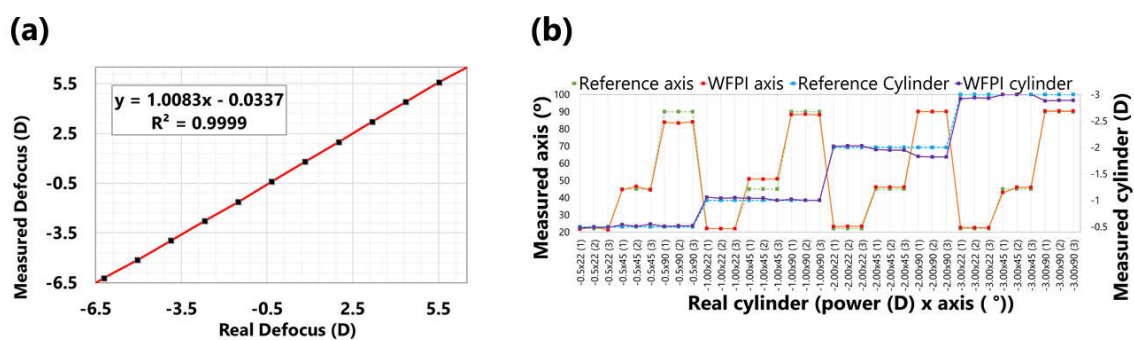
## 384 **Results**

---

### 385 **Calibration and validation**

386 The apparatus was able to recover the defocus introduced by the  
387 artificial eye with good precision, as shown in figure 3a. The error bars

388 are not visible because the standard deviation was very low in all cases.  
389 The mean error was  $0.04 \pm 0.06$  D (range [0.003 0.12]). Regarding the  
390 cylinder, introduced by means of +0.50, +1.00, +2.00 and +3.00 D  
391 cylindrical trial lenses with 90°, 45°, and 22° axes, the results are shown  
392 in figure 3b for all the measurement conditions. The mean absolute  
393 error in the cylinder power was  $0.05 \pm 0.05$  D (range [0 0.18]). The  
394 worst measurements were clearly those corresponding to the 2.00 D  
395 cylinder oriented at 90 degrees (error of  $0.18 \pm 0.005$  D). We do not  
396 know why these specific measurements were not as accurate as the  
397 rest of the measurements at 90 degrees or with the 2.00 D lens. The  
398 mean error in the axis orientation was  $1.67 \pm 2.06$  degrees (range [0  
399 6.6]). This seems reasonably accurate, as the trial lenses were oriented  
400 following a manual procedure using the pupil camera as a reference.  
401 Small angular differences between the science camera and the pupil  
402 camera could also explain this apparent inaccuracy.



403

404 Figure 3. Calibration of the apparatus for different induced defocuses  
405 and astigmatisms. (a) Defocus induced in artificial eyes with different  
406 axial lengths versus defocus recovered by the apparatus. (b) Different  
407 cylindrical trial lenses in different orientations and their measurement

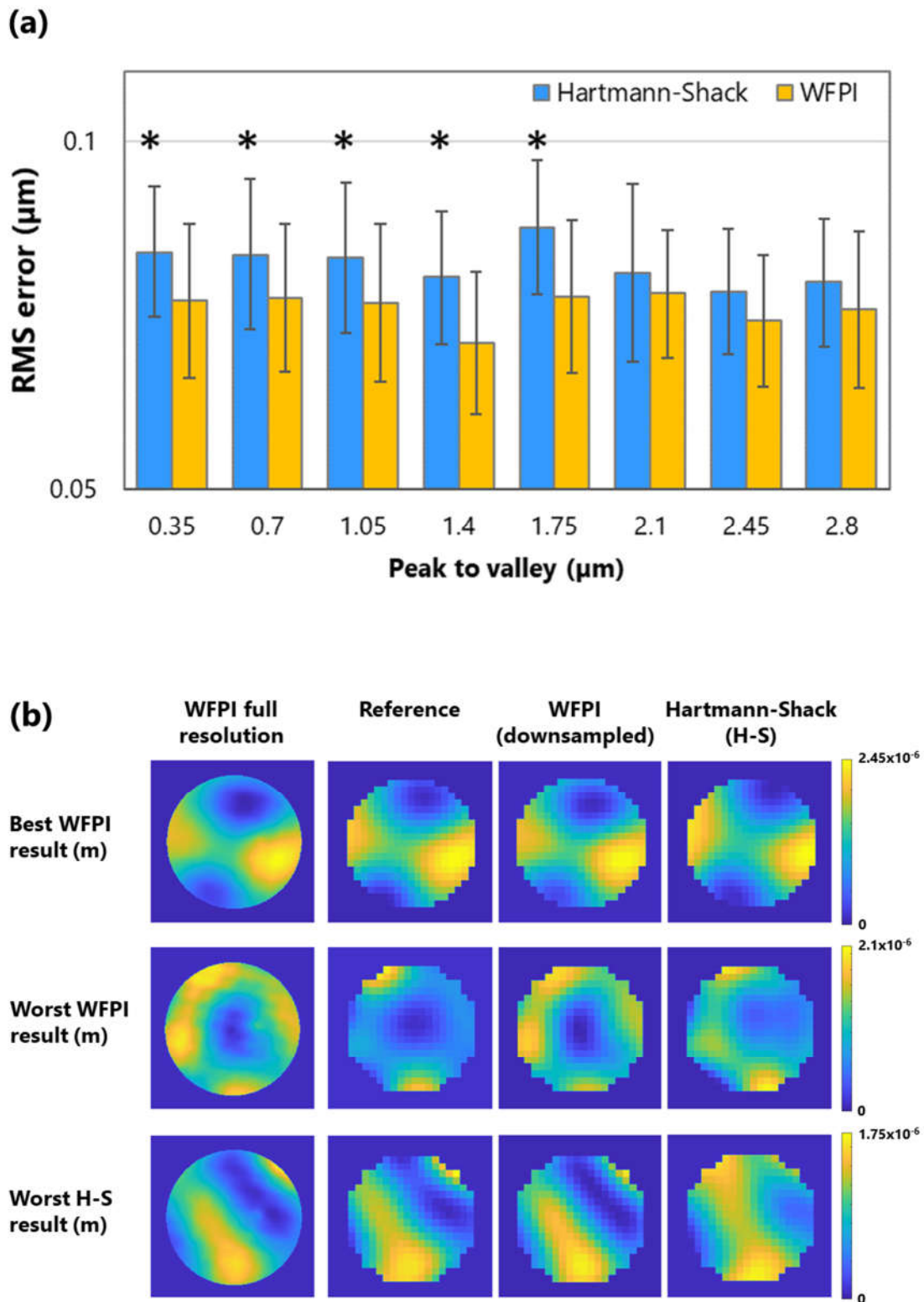
408 with the apparatus. Three different measurements were taken in each  
409 condition, and the data were for a 7 mm pupil diameter.

410 Calculations of the repeatability were performed using 100 consecutive  
411 measurements on an artificial eye with a 7 mm pupil diameter and  
412 yielded an average phase RMS of  $0.984 \pm 0.014 \mu\text{m}$ , with a maximum  
413 RMS difference between any two phase maps of  $0.063 \mu\text{m}$ . When the  
414 obtained phase maps were decomposed into the first 66 Zernike  
415 polynomials, the low-order RMS (Zernikes 3 to 5) was  $0.57 \pm 0.008 \mu\text{m}$ ,  
416 with a maximum difference of  $0.037 \mu\text{m}$ . The medium-order RMS  
417 (Zernikes 6 to 14) was  $0.051 \pm 0.004 \mu\text{m}$ , with a maximum difference of  
418  $0.019 \mu\text{m}$ . The high-order RMS (Zernikes 15 to 65) was  $0.01 \pm 0.001 \mu\text{m}$ ,  
419 with a maximum difference of  $0.005 \mu\text{m}$ .

420 The reproducibility calculations performed on 100 measurements on an  
421 artificial eye with a 7 mm pupil diameter yielded an RMS of  
422  $1.024 \pm 0.028 \mu\text{m}$ , with  $0.129 \mu\text{m}$  being the maximum difference  
423 between any two phase maps. When the obtained phase maps were  
424 decomposed into the first 66 Zernike polynomials, the low-order RMS  
425 (Zernikes 3 to 5) was  $0.599 \pm 0.02 \mu\text{m}$ , with a maximum difference of  
426  $0.092 \mu\text{m}$ . The medium-order RMS (Zernikes 6 to 14) was  $0.055 \pm 0.008$   
427  $\mu\text{m}$ , with a maximum difference of  $0.036 \mu\text{m}$ . The high-order RMS  
428 (Zernikes 15 to 65) was  $0.011 \pm 0.002 \mu\text{m}$ , with a maximum difference of  
429  $0.009 \mu\text{m}$ .

430 Figure 4 shows the validation of the apparatus in the presence of high  
431 frequencies induced by a DM for a 4 mm pupil diameter. The RMS  
432 error was calculated for each of the measurements by subtracting the

433 phase obtained with each sensor from the reference map. To make this  
434 operation possible, each measured phase map was resampled to the  
435 resolution of the reference map using bilinear interpolation. As shown  
436 in figure 4a, both sensors, the H-S and WFPI, showed similar behaviour,  
437 with the WFPI being statistically ( $p < 0.05$ ) more precise for amplitudes  
438 between 0.35 and 1.75  $\mu\text{m}$ . No significant outliers were observed in  
439 either of the two sensors. Small errors with respect to the reference  
440 map may be due to the resampling process by interpolation, or they  
441 may have a component associated with inaccuracies in the  
442 characterization of the response of the microactuators for complex  
443 input maps [25]. In figure 4b, the first row shows the case in which the  
444 WFPI sensor yielded its best result (amplitude or peak to valley (P-V)  
445 2.45  $\mu\text{m}$ ; RMS errors of 0.036 and 0.076  $\mu\text{m}$  for the WFPI and H-S  
446 sensors, respectively), while the second row shows its worst result (P-V  
447 2.1  $\mu\text{m}$ ; RMS errors of 0.202 and 0.124  $\mu\text{m}$  for the WFPI and H-S  
448 sensors, respectively). The third row shows the case in which the H-S  
449 sensor gave its worst result (P-V 1.75  $\mu\text{m}$ ; RMS errors of 0.048 and  
450 0.167  $\mu\text{m}$  for the WFPI and H-S sensors, respectively). We do not show  
451 the best case for the H-S sensor, since WFPI also showed a very good  
452 result (P-V 1.05  $\mu\text{m}$ ; RMS errors of 0.047 and 0.032  $\mu\text{m}$  for the WFPI  
453 and H-S sensors, respectively). The first column of figure 4b shows the  
454 result of the WFPI sensor at full resolution. When measured at a high  
455 resolution, a mesh-like lattice emerges as a background image, as seen  
456 in figure 4b. This background is compatible with the shape of the  
457 microactuators, so their individual influences on the phase can be  
458 estimated.



459

460 Figure 4. Instrument validation results using the WFPI sensor, a  
461 deformable mirror (DM), and a Hartmann-Shack sensor (H-S). (a) For a  
462 variety of different amplitudes or peak-to-valley values, the average

463 root-mean-square (RMS) errors of the residual phase map calculated  
464 by subtracting the measured phase maps from the reference maps and  
465 the error bars corresponding to the standard deviation are shown. An  
466 asterisk, \*, indicates a statistically significant difference between the  
467 two sensors (p-value <0.05). (b) The first row shows the case in which  
468 the WFPI sensor yielded its best result, the second row shows the case  
469 in which the WFPI sensor yielded its worst result, and the third row  
470 shows the case in which the H-S sensor yielded its worst result. The first  
471 column shows the high-resolution result of the WFPI sensor. The data  
472 are for a 4 mm pupil diameter.

#### 473 **In vivo test**

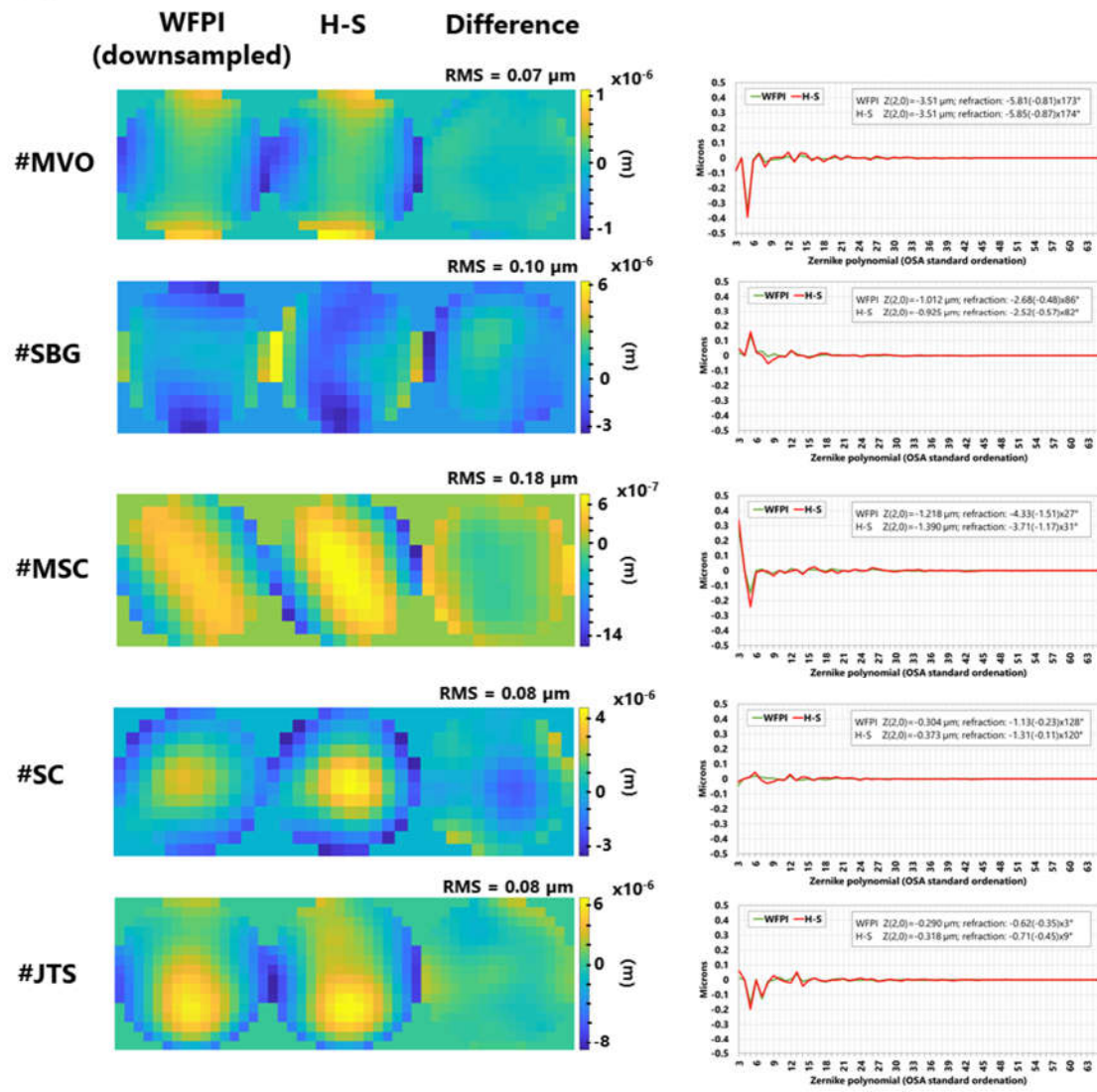
474 As a first step, repeatability/reproducibility was estimated in a  
475 real eye. It was a myopic eye with a spherical equivalent of  
476 approximately -6.21 D (eye #MVO in figures 5 and 6) and a naturally  
477 unusually large pupil size. 20 relatively consecutive measurements were  
478 taken. The subject was instructed to blink between measurements, with  
479 the approximate time between each being 3 seconds. As the  
480 measurements were performed without pharmacological dilation of the  
481 pupil, its diameter ranged from 7.3 to 7.7 mm during the test.  
482 Therefore, the analysis was restricted to a pupil diameter of 7.3 mm for  
483 all measurements. Piston and tip/tilt were removed from the  
484 measurements. The analysis of all obtained phase maps yielded a total  
485 RMS of  $11.028 \pm 0.32 \mu\text{m}$ , with the maximum difference between any  
486 two phase maps being  $1.25 \mu\text{m}$ . When the obtained phase maps were  
487 decomposed into the first 66 Zernike polynomials, the low-order RMS

488 (Zernikes 3 to 5) was  $6.198 \pm 0.196 \mu\text{m}$ , with a maximum difference of  
489  $0.801 \mu\text{m}$ . The medium-order RMS (Zernikes 6 to 14) was  $0.109 \pm 0.01$   
490  $\mu\text{m}$ , with a maximum difference of  $0.034 \mu\text{m}$ . The high-order RMS  
491 (Zernikes 15 to 65) was  $0.012 \pm 0.002 \mu\text{m}$ , with a maximum difference of  
492  $0.013 \mu\text{m}$ . These measurements can be understood as halfway between  
493 repeatability and reproducibility since accommodation is not paralyzed.  
494 Additionally, its activation could explain the variability in the total RMS  
495 and in the pupil diameter.

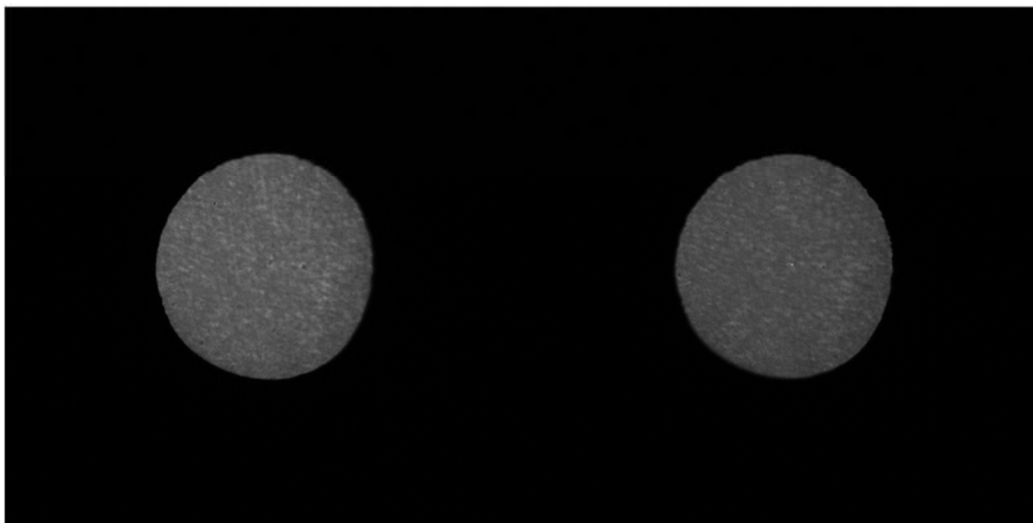
496 Figure 5a shows the comparative measurements of both sensors in the  
497 apparatus, the WFPI and H-S, for the 5 different real eyes, both as  
498 phase maps together with a difference map and in terms of the Zernike  
499 polynomial decomposition. In the latter, the defocus value (Zernike 4 or  
500  $Z(2,0)$ ) was set to zero to allow a better visualization of the graph, as  
501 defocus was the predominant component in almost all the eyes.  
502 Nevertheless, its value is shown in the data included in the graph,  
503 which also shows the spherocylindrical refraction of the eyes  
504 calculated from the data of both sensors. To make these comparisons,  
505 the WFPI measurement in circular pupils was resampled at the  
506 resolution of the H-S sensor. The differences in RMS between the two  
507 sensors were on the order of those observed during the device  
508 validation process. However, in eye #MSC, a clinically significant  
509 difference ( $>0.25 \text{ D}$ ) in refraction was detected in both the cylinder and  
510 defocus. We do not have a clear explanation of why this difference  
511 occurred, although we verified that our custom software for H-S data  
512 treatment detects high oblique astigmatisms poorly. Figure 5b shows  
513 an example of what the intensity images captured by the instrument

514 look like, corresponding to eye #MVO with a pupil diameter of 7.3 mm.  
515 Although we have not verified this, we believe that this type of intensity  
516 image could be useful in the diagnosis or monitoring of ocular  
517 pathologies that modify the amplitude, such as the presence of  
518 cataracts.

(a)



(b)



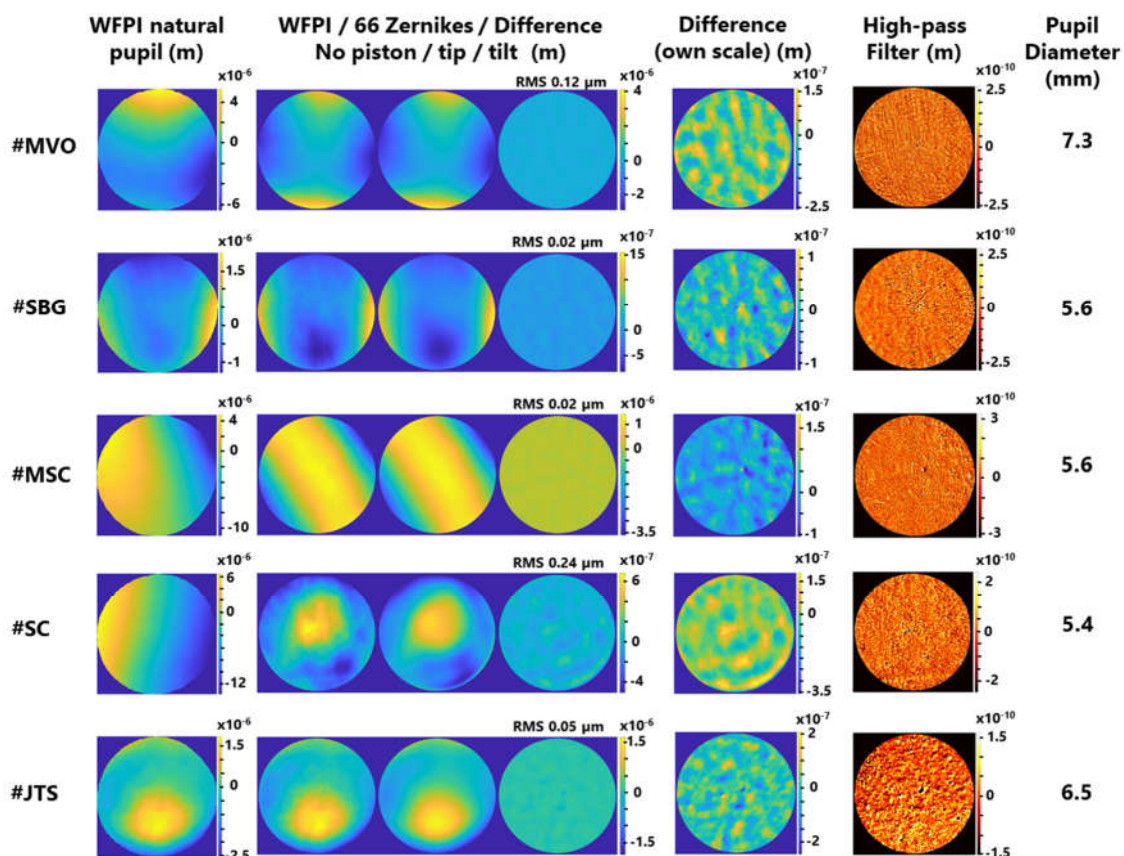
520 Figure 5. Measurements of 5 real eyes with the device. (a) Recovered  
521 phase map with the WFPI and with the H-S as well as its difference  
522 map together with its RMS value. On the right, the comparison of  
523 Zernike polynomials can be seen. For clarity, the defocus value (Zernike  
524 4) is set to zero on the graph, and the numerical value is provided,  
525 along with the sphero-cylindrical refraction, in the upper box of each  
526 individual graph. (b) Example of intensity images captured with the  
527 WFPI sensor, corresponding to eye #MVO.

528 All of the above leads us to figure 6, which is the main result of  
529 this work. These are the same eyes and measurements as those  
530 displayed in figure 5, but the entire phase maps were analysed in  
531 depth, making use of the whole available lateral resolution,  
532 approximately  $8.55 \mu\text{m}$ . The first column, labelled "WFPI natural pupil",  
533 shows the measurement result as it is returned by the apparatus. Note  
534 that this measurement was performed on the subject's natural pupil,  
535 which in no case turned out to be completely circular. As these  
536 measurements include the piston and tip/tilt, the details are masked by  
537 their high amplitudes. The second column, labelled "WFPI / 66 Zernikes  
538 / Difference", is made up of 3 sub-figures. The first sub-figure shows  
539 the previous result but within a circular pupil (the largest circular pupil  
540 inscribed within the natural pupil). In addition, the piston and tip/tilt  
541 have been removed. The second subfigure shows the fit to the first 66  
542 Zernike polynomials. The third sub-figure shows the difference  
543 between the two previous phase maps together with its RMS. The third  
544 column, labelled "Difference (own scale)", shows the difference  
545 between the phase map adjusted to Zernikes and without the

546 adjustment with its own colour map, that is, the third sub-figure of  
547 column 2 but with its own scale. This last image represents the  
548 information that cannot be captured with a decomposition in terms of  
549 the first 66 Zernike polynomials (similar to the information that is  
550 usually provided by commercial aberrometers) and is the main  
551 contribution of this work. In all cases, a substructure of peaks and  
552 valleys emerges with an approximate amplitude between 200 and 300  
553 nm. The case of eye #SC is remarkable, as there were 0.24 microns of  
554 RMS that could not be characterized with a decomposition in terms of  
555 the first 66 Zernike polynomials, which is a significant quantity for the  
556 human eye. Finally, the last column, labelled "High-pass filter", shows  
557 the result of the first sub-image of the second column, to which a  
558 Gaussian filter of sigma 0.5 was applied to reveal the high-frequency  
559 components of the phase map. There were notable differences  
560 between the 5 eyes. While some sort of vertical line is observed in eye  
561 #MVO (the most myopic), this pattern is not present in the rest of the  
562 eyes. Although we cannot be sure of the origin of these lines, they are  
563 compatible with the molecular arrangement of some macular  
564 components, such as the xanthophilic pigment of the macula lutea,  
565 which is arranged in parallel lines [26], and this could have somehow  
566 been transmitted to the recovered phase map. Its origin could also be  
567 originated in tensions of the posterior capsule. Future studies will be  
568 necessary to clarify the origin of these lines, since we have already  
569 ruled out instrumental effects. In eye #SBG, a filamentous structure  
570 with an amplitude on the order of 0.4 nm can be seen that would be  
571 compatible with a floater in the vitreous body. Eye #JTS, the most

572 emmetropic, is perhaps the most striking due to its differences with  
573 respect to the rest, since a mottling can be observed that covers the  
574 entire pupil. We hypothesize that this finding may be related to some  
575 degree of dry eye. Applying high-pass filters is somewhat tricky, and  
576 different filters can be applied that reveal different phase components.  
577 We applied this filter specifically because we think it reveals the  
578 underlying structure well in most eyes. However, for the interested  
579 reader, we provide the raw phase maps as additional data (column 1 of  
580 figure 6). We encourage alternative analyses.

581



582

583 Figure 6. Measurements of 5 real eyes (the same as in figure 5) with the  
584 device and its analysis with a lateral resolution of 8.55 microns. The first

585 column is the phase map retrieved by the apparatus. The second  
586 column is a group of 3 sub-images comprising the WFPI result within a  
587 circular pupil and without piston/tip/tilt, its fit to the first 66 Zernike  
588 polynomials, and the difference between the two. The third column is  
589 the same difference phase map as above but with its own colour map  
590 or scale. The fourth column is the first phase map of the second  
591 column, to which a Gaussian filter with  $\sigma = 0.5$  was applied, thus  
592 revealing the high-frequency components of the phase. Finally, the last  
593 column indicates the diameter of the pupil when considering a circular  
594 pupil (the largest inscribed pupil).

595

## 596 Discussion

---

597 In this work, we provided strong evidence that ocular optics are more  
598 complex than previously assumed and, below the previous resolution  
599 limits, there is a large amount of information that until now has been  
600 unknown. To visualize the optics with a lateral resolution of  
601 approximately  $8.55 \mu\text{m}$ , we used a relatively new phase sensor, the  
602 WFPI sensor. An exhaustive calibration and validation of the WFPI with  
603 the apparatus was carried out, focusing on ocular measurements, using  
604 all the tools at our disposal, and improving (by including more tests)  
605 the methodology used for the validation of other ocular aberrometer  
606 proposals. [9, 27]. At this point, it should not matter which phase  
607 sensor is used, and in fact, the same results should be obtained using  
608 any other sensor (i.e., H-S) adapted to measure with a similar

609 resolution, perhaps in smaller areas within the pupil to be able to  
610 achieve this lateral resolution.

611 In this small sample of 5 healthy eyes, an optical structure in the  
612 200-300 nm range was clearly revealed in all cases. Since the phase  
613 map represents the integration of all ocular structures, it is still too  
614 early to say exactly where this structure comes from. The next step will  
615 be the construction of a prototype capable of measuring in real time  
616 (we have had difficulties in getting a camera capable of measuring in  
617 real time with the characteristics of the one used.) In this way, in  
618 combination with cycloplegia or not or by measuring pseudophakic  
619 patients, it could be estimated whether this structure comes from the  
620 tear, the lens, the cornea, other ocular media, or the retina. However, in  
621 the repeatability measurements for the real eyes, this pattern was  
622 consistent among all measures, suggesting that it did not come from  
623 the tear. When a high-pass filter was applied, another series of details  
624 were revealed, different for each eye, for which we still do not have a  
625 clear explanation. Especially striking is the case of the most myopic eye,  
626 #MVO, where a series of parallel and vertical lines appeared that cross  
627 the pupil.

628 The scope of this discovery is unknown. Most likely, it will take  
629 years of clinical studies to learn how to interpret this new information,  
630 associate it with different pathologies or conditions, and determine  
631 whether it has a real clinical application or is just a curiosity. The  
632 applications of ocular aberrometry are ubiquitous: they include  
633 refractive surgery (i.e., LASIK) [28], the diagnosis and monitoring of

634 diseases [29], myopia control [30], intraocular lenses [31], light-  
635 adjustable intraocular lenses [32], objective refraction [33],  
636 intraoperative aberrometry [34], and vision science [35]. Additionally,  
637 combining a wavefront sensor with a compensating element, such as a  
638 liquid crystal spatial light modulator, has dramatically improved in vivo  
639 observations of the human retina [36]. It has also enabled the  
640 possibility of improved visual perception, so-called super-vision, which  
641 is a visual acuity far beyond the normal values [37]. Although all of  
642 these are potential applications of this finding, it would be pure  
643 speculation to say at this point that it will have a significant impact on  
644 any of them (however, we are optimistic about it).

645         It is important to note that we are not using a commercial H-S  
646 sensor built expressly for ophthalmic measurements but a general-  
647 purpose sensor. Additionally, resampling the high-resolution phase  
648 map to the H-S resolution may not exactly represent what an H-S  
649 sensor would detect. We believe that the small differences between the  
650 measurements of the two sensors can be justified in this way. While  
651 different approaches could be taken to improve this aspect, especially  
652 regarding interpolation, it would be difficult to justify this, as such  
653 approaches would appear purposefully made to make the results  
654 appear accurate. For this reason, we preferred to perform a simple  
655 bilinear interpolation for the comparisons. We believe that the  
656 existence of differences between the two sensors after an exhaustive  
657 validation of WFPI is also valuable information, and it may be behind  
658 the typical errors of H-S sensors applied in ophthalmology. [38-41].  
659 However, analysing in detail what the H-S is not capable of detecting

660 would deviate too much from the main objective of this work, which is  
661 to show the phase map of the human eye with high lateral resolution,  
662 and it will be the subject of future studies.

663

## 664 **Conclusion**

---

665 In this work, we showed that when the optics of the human eye  
666 are measured at a lateral resolution of 8.55  $\mu\text{m}$ , a series of optical  
667 substructures with a pattern of peaks and valleys that appear in an  
668 amplitude range of 200 to 300 nm are revealed. Furthermore, the  
669 phase map of the human eye was shown to be rich in high frequencies  
670 when a high-pass filter is applied to the result at a high resolution. This  
671 is the first time this finding has been described, and it could have a  
672 significant impact on our understanding of some fundamental  
673 mechanisms of human vision as well as outstanding utility in certain  
674 fields of ophthalmology.

675

## 676 **References**

---

- 677 1. Scheiner, C. *Oculus, hoc est: Fundamentum Opticum*. Flesher.  
678 Oeniponti, Innsbruck, Austria (1619).
- 679 2. Smirnov, M. S. Measurement of wave aberration in the human  
680 eye. *Biophysics (English Translation of Biofizika)*, 6, 52-64 (1961).
- 681 3. Thibos, L. N. Principles of Hartmann-Shack aberrometry. *J. Refract.*  
682 *Surg.*, 16 S563-565 (2000).

- 683 4. Chiesa, S., & Dainty, J. C. Calibration and performance of a pyramid  
684 wavefront sensor for the eye. *J. Mod. Opt.*, 59(16), 1415-1427 (2012).
- 685 5. Szczesna, D. H., Alonso-Caneiro, D., Iskander, D. R., Read, S. A., &  
686 Collins, M. J. Lateral shearing interferometry, dynamic wavefront  
687 sensing, and high-speed videokeratoscopy for noninvasive assessment  
688 of tear film surface characteristics: a comparative study. *J. Biomed. Opt.*,  
689 15(3), 037005 (2010).
- 690 6. Navarro, R., & Losada, M. A. Aberrations and relative efficiency of  
691 light pencils in the living human eye. *Optom. Vis. Sci.*, 74(7), 540-547  
692 (1997).
- 693 7. Díaz-Doutón, F., Pujol, J., Arjona, M., & Luque, S. O. Curvature sensor  
694 for ocular wavefront measurement. *Opt. Lett.*, 31(15), 2245-2247 (2006).
- 695 8. Plaza-Puche, A. B., Salerno, L. C., Versaci, F., Romero, D., & Alio, J. L.  
696 Clinical evaluation of the repeatability of ocular aberrometry obtained  
697 with a new pyramid wavefront sensor. *Eur. J. Ophthalmol.*, 29(6), 585-  
698 592 (2019).
- 699 9. Cheng, X., Himebaugh, N. L., Kollbaum, P. S., Thibos, L. N., & Bradley,  
700 A. Validation of a clinical Shack-Hartmann aberrometer. *Optom. Vis.*  
701 *Sci.*, 80(8), 587-595 (2003).
- 702 10. Wu, Y., He, J. C., Zhou, X. T., & Chu, R. Y. A limitation of Hartmann-  
703 Shack system in measuring wavefront aberrations for patients received  
704 laser refractive surgery. *PloS one*, 10(2), e0117256 (2015).

- 705 11. Shatokhina, I., Hutterer, V., & Ramlau, R. Review on methods for  
706 wavefront reconstruction from pyramid wavefront sensor data. *J.*  
707 *Astron. Telesc. Instruments, Syst.*, 6(1), 010901 (2020).
- 708 12. M. Born and E. Wolf, *Principles of Optics* (Pergamon, New  
709 York, 1975), Sec. 9.2 (1999).
- 710 13. Porter, J., Guirao, A., Cox, I. G., & Williams, D. R. Monochromatic  
711 aberrations of the human eye in a large population. *J. Opt. Soc. Am. A.*,  
712 18(8), 1793-1803 (2001).
- 713 14. del Águila Carrasco, A. J., Taboada, J. J. E., Albert, N. M., Romín, D.  
714 M., & Micó, R. M. Fitting Zernike polynomials to ocular wavefront  
715 aberrations. Effect of the radial order on the fitting accuracy. *J.*  
716 *Emmetropia*, 6(2), 87-90 (2015).
- 717 15. Carvalho, L. A. Accuracy of Zernike polynomials in characterizing  
718 optical aberrations and the corneal surface of the eye. *Invest.*  
719 *Ophthalmol. Vis. Sci.*, 46(6), 1915-1926 (2005).
- 720 16. Llorente, L., Marcos, S., Dorronsoro, C., & Burns, S. A. Effect of  
721 sampling on real ocular aberration measurements. *J. Opt. Soc. Am. A.*,  
722 24(9), 2783-2796 (2007).
- 723 17. Klyce, S. D., Karon, M. D., & Smolek, M. K. Advantages and  
724 disadvantages of the Zernike expansion for representing wave  
725 aberration of the normal and aberrated eye. *J. Refract. Surg.*, 20(5),  
726 S537-S541 (2004).
- 727 18. Trujillo-Sevilla, J. M., Gonzalez, O. C., Bonaque-González, S.,  
728 Gaudestad, J., & Ramos, J. R. High-resolution wave front phase sensor

729 for silicon wafer metrology. In Photonic Instrumentation Engineering VI  
730 (Vol. 10925, p. 109250I). International Society for Optics and Photonics  
731 (2019).

732 19. Talmi, A., & Ribak, E. N. Wavefront reconstruction from its  
733 gradients. *J. Opt. Soc. Am. A.*, 23(2), 288-297 (2006).

734 20. Ceruso, S., Bonaque-González, S., Pareja-Ríos, A., Carmona-  
735 Ballester, D., & Trujillo-Sevilla, J. Reconstructing wavefront phase from  
736 measurements of its slope, an adaptive neural network based  
737 approach. *Opt. Lasers. Eng.*, 126, 105906 (2020).

738 21. Rodríguez-Ramos, JM., Lüke, JP., Trujillo-Sevilla, JM., & Fernández-  
739 Valdivia JJ. Method for determining the complex amplitude of the  
740 electromagnetic field associated with a scene. Worldwide patent  
741 PCT/ES2015/070936 (2015).

742 22. Delori, F. C., Webb, R. H. & Sliney, D. H. Maximum permissible  
743 exposures for ocular safety (ANSI 2000), with emphasis on ophthalmic  
744 devices. *J. Opt. Soc. Am. A.*, 24(5), 1250–1265 (2007).

745 23. Salmon, T. O., West, R. W., Gasser, W., & Kenmore, T. Measurement  
746 of refractive errors in young myopes using the COAS Shack-Hartmann  
747 aberrometer. *Optom. Vis. Sci.*, 80(1), 6-14 (2003).

748 24. Thibos LN, Applegate RA, Schwiegerling JT, Webb RH. Members  
749 VST Standards for reporting the optical aberrations of eyes. Vision  
750 Science and its Applications TOPS Volume. 2000.35.

- 751 25. Horsley, D. A., Park, H., Laut, S. P., & Werner, J. S. Characterization of  
752 a bimorph deformable mirror using stroboscopic phase-shifting  
753 interferometry. *Sens. Act. A: Physical*, 134(1), 221-230 (2007).
- 754 26. Ahmed, S. S., Lott, M. N., & Marcus, D. M. The macular xanthophylls.  
755 *Surv. Ophthalmol.*, 50(2), 183-193 (2005).
- 756 27. Singh, N. K., et al. Validation of a clinical aberrometer using  
757 pyramidal wavefront sensing. *Optom. Vis. Sci.*, 96(10), 733-744 (2019).
- 758 28. Uceda-Montañés, A., Rogers, M., & Piñero, D. P. Visual and  
759 refractive outcomes with a new topography-integrated wavefront-  
760 guided lasik procedure. *Curr. Eye Res.*, 1-7 (2020).
- 761 29. Markoulli, M., et al. Clinical utility of irx3 in keratoconus. *Clin. Exp.*  
762 *Optom.* (2020).
- 763 30. Vincent, S. J., et al. Higher order aberrations and axial elongation in  
764 combined 0.01% atropine with orthokeratology for myopia control.  
765 *Ophthalmic. Physiol. Opt.*, 40(6), 728-737 (2020).
- 766 31. Bonaque-González, S., Ríos, S., Amigó, A., & López-Gil, N. Influence  
767 on visual quality of intraoperative orientation of asymmetric intraocular  
768 lenses. *J. Refract. Surg.*, 31(10), 651-657 (2015).
- 769 32. Patnaik, J. L., & Kahook, M. Y. Long-term follow-up and clinical  
770 evaluation of the light-adjustable intraocular lens implanted after  
771 cataract removal: 7-year results. *J. Cataract. Refract. Surg.*, 46(6), 929  
772 (2020).

- 773 33. Fu, D., Ding, X., Shang, J., Yu, Z., & Zhou, X. Accuracy of WASCA  
774 aberrometer refraction compared to manifest refraction and  
775 cycloplegic refraction in hyperopia measurement. *Transl. Vis. Sci.*  
776 *Technol.*, 9(11), 5-5 (2020).
- 777 34. Page, T. P. Intraoperative wavefront aberrometry to determine  
778 planar endpoint for the repositioning of vaulted accommodative  
779 intraocular lenses. *J. Cataract. Refract. Surg.* (2020).
- 780 35. Bonaque-González, S., Ríos-Rodríguez, S., & López-Gil, N.  
781 Improving vision by pupil masking. *Biomed. Opt. Express.*, 7(7), 2538-  
782 2550 (2016).
- 783 36. Li, W., et al. Quality improvement of adaptive optics retinal images  
784 using conditional adversarial networks. *Biomed. Opt. Express.*, 11(2),  
785 831-849 (2020).
- 786 37. Sabesan, R., & Yoon, G. Visual performance after correcting higher  
787 order aberrations in keratoconic eyes. *J. Vis.*, 9(5), 6-6 (2009).
- 788 38. Visser, N., Berendschot, T. T., Verbakel, F., Tan, A. N., de Brabander,  
789 J., & Nuijts, R. M. Evaluation of the comparability and repeatability of  
790 four wavefront aberrometers. *Investig. Ophthalmol. Vis. Sci.*, 52(3),  
791 1302-1311 (2011).
- 792 39. Mirshahi, A., Bühren, J., Gerhardt, D., & Kohnen, T. In vivo and in  
793 vitro repeatability of Hartmann-Shack aberrometry. *J. Cataract. Refract.*  
794 *Surg.*, 29(12), 2295-2301 (2003).

795 40. Burakgazi, A. Z., Tinio, B., Bababyan, A., Niksarli, K. K., & Asbell, P.  
796 Higher order aberrations in normal eyes measured with three different  
797 aberrometers. *J. Refract. Surg.*, 22(9), 898-903 (2006).

798 41. López-Miguel, A., et al. Precision of a commercial Hartmann-Shack  
799 aberrometer: limits of total wavefront laser vision correction. *Am. J.*  
800 *Ophthalmol.*, 154(5), 799-807 (2012).

801

## 802 **Acknowledgements**

---

803 We thank José Luis Hernández-Afonso for his administrative and  
804 logistical assistance. We thank Jan Gaudestad for a critical review of the  
805 manuscript.

806

## 807 **Author contributions**

---

808 S.B.G. contributed to all stages of the project. J.M.T.S. contributed to all  
809 stages of the project. M.V.O. contributed to all stages of the project  
810 except the development of the WFPI algorithm. O.C.G. contributed as  
811 the main computer engineer. M.S.C. contributed as the main electronic  
812 engineer. A.R.V. contributed as the main mechanical engineer. S.C.  
813 contributed to the development of the WFPI algorithm. R.O.G.  
814 contributed to the processing software and hardware control. J.M.H.  
815 contributed to the hardware control. O.G.C. contributed to the  
816 hardware control. J.G.M.H. contributed to the processing software. D.G.  
817 contributed to the interpretation of data. J.T.H. contributed to the

818 interpretation of data. J.M.R.R. contributed to the development of the  
819 WFPI algorithm and to the conception and design of the work.

820

## 821 **Additional information**

---

822 The data used to generate figure 6 are included for anyone to  
823 use at [https://bitbucket.org/wooptix/wfpi\\_data](https://bitbucket.org/wooptix/wfpi_data). The rest of the data  
824 generated or analysed during this study are included in this published  
825 article. These additional data are available from the corresponding  
826 author upon reasonable request.

827 The authors declare the following competing interests:

828 S.B.G., employment. J.M.T.S., employment. M.V.O., employment. O.C.G.,  
829 employment. M.S.C., employment. A.R.V., employment. S.C.,  
830 employment. R.O.G., employment. J.M.H., employment. O.G.C.,  
831 employment. J.G.M.H., employment. D.G., personal financial interests.  
832 J.T.H., personal financial interests. J.M.R.R., personal financial interests.